Available online at www.sciencedirect.com
ScienceDirect
Photonics and Nanostructures – Fundamentals and Applications 7 (2009) 2–11
PHOTONICS AND NANOSTRUCTURES Fundamentals and Applications
www.elsevier.com/locate/photonics

Higher-order time-domain methods for the analysis of nano-photonic systems

Jens Niegemann, Michael König, Kai Stannigel, Kurt Busch *

Institut für Theoretische Festkörperphysik, Universität Karlsruhe (TH), 76128 Karlsruhe, Germany

Received 28 June 2008; accepted 20 August 2008
Available online 9 September 2008

Abstract

In thiswork, we investigate the use of higher-order Discontinuous Galerkin (DG) methods for time-domain computations of nano-photonic systems. We briefly discuss the implementation of such methods and comment on several important extensions such as Perfectly Matched Layers (PMLs), sources and dispersive materials. In particular, we propose a novel way to accurately implement delta-like point sources and we present a detailed study on the performance of PMLs within the DG framework. We demonstrate that the PML-performance may be substantially improved through an appropriate choice of the absorption profile. Finally, we employ our specific version of the DG method to certain plasmonic systems such as silver cylinders and nano-structured metallic films.

PACS : 02.60.Cb; 02.70.Dh; 42.25.Bs; 42.25.Fx

Keywords: Maxwell equations; Discontinuous Galerkin; Time-domain calculations

1. Introduction

Time-domain computations play a very prominent role in the characterization and design of micro- and nano-photonic structures. In these structures, strong multiple scattering and/or near-field effects allow a far reaching control over the propagation characteristics of light and its interaction with matter. Important systems that are currently being investigated include but are not limited to periodic nano-structures and plasmonic elements and we would like to refer the reader to a number recent reviews [1–3].

Among the various methods for time-domain computations of Maxwell's equations, the Finite-Difference Time-Domain (FDTD) method [4] stands out for its efficiency and versatility. In fact, several powerful packages, commercial and open-source, are available. In essence, the basic FDTD method represents a conditionally stable algorithm with second order accuracy in space and time. Within this approach, the Maxwell curl-equations are discretized such that electric and magnetic fields are, respectively, evaluated on a uniform and staggered spatial grid, the so-called Yee grid. Consequently, the time-stepping is realized via an explicit leapfrog scheme. This apparent simplicity lies at the heart of the methods' efficiency but, at the same time, also represents a serious limitation. In particular, the accurate treatment of material interfaces that are not grid-aligned is a serious concern and, for linear optics, advanced methods have been developed very recently [5–8]. However, these methods either reduce the efficiency of the basic algorithm [5,6] or it is presently unclear how

* Corresponding author.
E-mail address: kurt@tfp.uni-karlsruhe.de (K. Busch).

1569-4410/$ – see front matter © 2008 Elsevier B.V. All rights reserved.
doi:10.1016/j.photonics.2008.08.006

to extend them to three dimensions [7,8]. None of these approaches allows to deal with situations that involve materials with appreciable nonlinear properties. Furthermore, even for the linear optics of curved interfaces between metals and dielectrics, notable problems, mostly associated with spurious field enhancements, remain.

On the other hand, accurate representation of arbitrary interfaces and high-order spatial discretization are the trademarks of finite-element methods [9]. Despite these apparent advantages, there exists one essential drawback that has prevented traditional finite-element methods from becoming mainstream in large-scale time-domain computations: The resulting time-stepping algorithms are implicit so that at every time-step a (typically large) system of equations has to be solved. In other words, the CPU-times associated with traditional finite-element time-domain computations quickly become prohibitively large even for systems of moderate size.

However, the past years have witnessed dramatic progress when discontinuous Galerkin (DG) finite-element techniques have been applied to Maxwell's equations [10]. As we will detail below, this approach combines the attractive features of finite-elements with explicit time-stepping capabilities. In particular, the generic treatment of arbitrary interfaces in combination with high-order discretizations both in space and time leads to performance characteristics that are ideally suited for applications in nano-photonic systems. More precisely, in Section 2, we sketch the essentials of the DG Time-Domain (DGTD) approach. We then report on important add-ons for realistic applications such as the treatment of open systems, point sources, and dispersive media in Section 3. In particular, to the best of our knowledge, this is the first time that an accurate treatment of point sources within DGTD has been described. In Section 4, we provide a detailed study of Perfectly Matched Layers boundary conditions and obtain DGTD-optimized absorption profiles. This also allows us to compare the performance of DGTD and standard FDTD. Finally, we will – in Section 5– apply our DGTD implementation to the important problem of extraordinary transmission through subwavelength apertures in nano-structured metallic films.

2. The discontinuous Galerkin method

For the numerical calculations, we employ a DG method in the nodal formulation of Hesthaven and Warburton [10]. To keep the discussion brief, it is convenient to express Maxwell's equations in a conservation form

$$\partial_t(\mathcal{Q}(\vec{r})\mathbf{q}(\vec{r},t)) + \nabla\cdot\vec{F}(\mathbf{q}) = 0, \tag{1}$$

where the material matrix $\mathcal{Q}(\vec{r})$, the field vector $\mathbf{q}$ and the flux vector $\vec{F}(\mathbf{q}) = (\mathbf{F}_1(\mathbf{q}), \mathbf{F}_2(\mathbf{q}), \mathbf{F}_3(\mathbf{q}))^{\mathrm{T}}$ are defined as

$$\mathcal{Q}(\vec{r}) = \begin{pmatrix} \epsilon(\vec{r}) & 0 \\ 0 & \mu(\vec{r}) \end{pmatrix}, \mathbf{q}(\vec{r},t) = \begin{pmatrix} \vec{E}(\vec{r},t) \\ \vec{H}(\vec{r},t) \end{pmatrix},$$

$$\text{and} \quad \mathbf{F}_i(\mathbf{q}) = \begin{pmatrix} -\hat{e}_i \times \vec{H}(\vec{r},t) \\ \hat{e}_i \times \vec{E}(\vec{r},t) \end{pmatrix}.$$

In these expressions, $\hat{e}_i$, $i = 1,2,3$ denote the Cartesian unit vectors. In order to solve this system, the computational domain is tessellated into K conforming elements Ω^k. Typically, these elements will be triangles in two dimensions and tetrahedra in three dimensions. On each element, the fields are then expanded in terms of interpolating Lagrange polynomials $L_i(\vec{r})$

$$\mathbf{q}^k(\vec{r},t) \approx \sum_{i=1}^{N} \mathbf{q}^k(\vec{r}_i,t)L_i(\vec{r}) = \sum_{i=1}^{N} \tilde{\mathbf{q}}_i^k(t)L_i(\vec{r}), \tag{2}$$

where N denotes the number of coefficients that have been utilized. For triangles, this number is connected to the polynomial expansion order n via $N_{\mathrm{Tri}} = (n+1)(n+2)/2$ while for tetrahedra the corresponding dependence is $N_{\mathrm{Tet}} = (n+1)(n+2)(n+3)/6$. The vector $\tilde{\mathbf{q}}^k(t)$ contains the unknown field values that have to be solved for. A suitable set of interpolation nodes $\vec{r}_i$ can, for instance, be obtained via the method proposed in Ref. [11].

The standard Galerkin approach consists in multiplying Eq. (1) with $L_i(\vec{r})$ and integrating over an element Ω^k, which yields

$$\int_{\Omega^k} (\mathcal{Q}^k\partial_t\tilde{\mathbf{q}}^k + \nabla\cdot\vec{F}(\tilde{\mathbf{q}}^k))L_i(\vec{r})\,\mathrm{d}\vec{r} = 0.$$

To facilitate the coupling with neighboring cells, the next step is to employ an integration by parts and to substitute in the resulting contour integral the physical flux $\vec{F}(\tilde{\mathbf{q}}^k(t))$ with a so-called numerical flux $\vec{F}^*(\tilde{\mathbf{q}}^k(t))$. A second integration by parts then results in the strong formulation

$$\int_{\Omega^k} (\mathcal{Q}^k\partial_t\tilde{\mathbf{q}}^k + \nabla\cdot\vec{F}(\tilde{\mathbf{q}}^k))L_i(\vec{r})\,\mathrm{d}\vec{r}$$

$$= \int_{\partial\Omega^k} \hat{\mathrm{n}}\cdot(\vec{F}(\tilde{\mathbf{q}}^k) - \vec{F}^*(\tilde{\mathbf{q}}^k))L_i(\vec{r})\,\mathrm{d}\vec{r}, \tag{3}$$

where $\hat{\mathrm{n}}$ is the outward-pointing normal vector of the contour. In Ref. [10], it has been proved that this

procedure results in a stable and convergent scheme if the numerical flux $\vec{F}^*(\tilde{\mathbf{q}}^k(t))$ is chosen properly. One suitable choice is the well established upwinding flux [10] which leads to the expression

$$\hat{\mathrm{n}} \cdot (\vec{F}(\tilde{\mathbf{q}}^k) - \vec{F}^*(\tilde{\mathbf{q}}^k)) = \begin{pmatrix} \dfrac{(\Delta\vec{E} - \hat{n}\cdot(\hat{n}\cdot\Delta\vec{E}) + Z^+\hat{n}\times\Delta\vec{H})}{\bar{Z}} \\ \dfrac{(\Delta\vec{H} - \hat{n}\cdot(\hat{n}\cdot\Delta\vec{H}) - Y^+\hat{n}\times\Delta\vec{E})}{\bar{Y}} \end{pmatrix}. \tag{4}$$

Here, $\Delta\vec{E} = \vec{E}^+ - \vec{E}^-$ and $\Delta\vec{H} = \vec{H}^+ - \vec{H}^-$ denote the difference of the fields across the cell interface, and the superscript "+" denotes the neighboring element while the superscript"−" refers to the local cell. Further, we have introduced cell-impedances $Z^\pm = \sqrt{\mu^\pm}/\sqrt{\epsilon^\pm}$ and -conductances $Y^\pm = 1/Z^\pm$ together with corresponding summed values $\bar{Y} = Y^+ + Y^-$ and $\bar{Z} = Z^+ + Z^-$. Several types of relevant boundary conditions can be applied by setting the material parameters at the outer cell to $Z^+ = Z^-$ and by defining $\Delta\vec{E}$ and $\Delta\vec{H}$ according to the following table:

Boundary condition	$\Delta\vec{E}$	$\Delta\vec{H}$
Perfect electric conductor (PEC)	$-2\vec{E}^-$	0
Perfect magnetic conductor (PMC)	0	$-2\vec{H}^-$
Silver-Müller (1st order absorbing)	$-2\vec{E}^-$	$-2\vec{H}^-$

Explicit expressions for the fields are obtained by inserting the expansions (2) together with the numerical fluxes from Eq. (4) into Eq. (3). If we assume constant material parameters ϵ^k, μ^k within each element we find after certain algebraic transformations

$$\epsilon^k \frac{\partial\vec{E}^k}{\partial t} = \vec{D}^k \times \vec{H}^k + (\mathcal{M}^k)^{-1}\mathcal{F}^k\left(\frac{\Delta\vec{E} - \hat{n}\cdot(\hat{n}\cdot\Delta\vec{E}) + Z^+\hat{n}\times\Delta\vec{H}}{\bar{Z}}\right), \tag{5}$$

$$\mu^k \frac{\partial\vec{H}^k}{\partial t} = -\vec{D}^k \times \vec{E}^k + (\mathcal{M}^k)^{-1}\mathcal{F}^k\left(\frac{\Delta\vec{H} - \hat{n}\cdot(\hat{n}\cdot\Delta\vec{H}) - Y^+\hat{n}\times\Delta\vec{E}}{\bar{Y}}\right). \tag{6}$$

To streamline the notation, we have introduced the vectors $\vec{E}^k$ and $\vec{H}^k$, where each component is a N-vector of the respective field values in element k. Furthermore, we have defined a vector of differentiation matrices $\vec{D}^k = (\mathcal{D}_x^k, \mathcal{D}_y^k, \mathcal{D}_z^k)$, the mass matrix $\mathcal{M}^k$, and the face matrix $\mathcal{F}^k$ according to

$$(\mathcal{D}_m^k)_{ij} = \partial_m L_j(\vec{r}_i) \quad \text{with} \quad m \in \{x, y, z\},$$

$$(\mathcal{M}^k)_{ij} = \int_{\Omega^k} L_i(\vec{r}) L_j(\vec{r})\, \mathrm{d}\vec{r},$$

$$(\mathcal{F}^k)_{ij} = \int_{\partial\Omega^k} L_i(\vec{r}) L_j(\vec{r})\, \mathrm{d}\vec{r} \quad \text{where} \quad j \in \{\, j | \vec{r}_j \in \partial\Omega^k \}.$$

The remaining step of integrating the semi-discrete system (5) and (6) in time is executed through a 4th-order low-storage Runge–Kutta scheme as described in Ref. [12]. Since the foregoing procedure is explicit, a Courant-Friedrichs-Levy (CFL) criterion has to be fulfilled in order to guarantee stability. In practice, we limit the time-step according to

$$\Delta t \leq c_{\mathrm{CFL}}\, d_{\min} \min_k (r_{\mathrm{in}}^k), \tag{7}$$

where $d_{\min}$ is the minimal distance between two interpolation nodes $\vec{r}_i$. Furthermore, r_{in}^k denotes the radius of the incircle or insphere of element k and c_{CFL} is a number of the order one. Its critical value can only be obtained empirically and depends on the dimensionality of the system as well as on the expansion order. However, the value $c_{\mathrm{CFL}} = 1$ leads to stable results in all of our calculations. It should be noted that the reduced performance due to the CFL criterion can be improved upon by using more advanced integration methods such as those described in Refs. [13–15].

3. Implementation of PMLs, point sources and dispersive media

In order to properly model nano-photonic systems, certain extensions to the bare numerical scheme are required. A first relevant aspect is the implementation of absorbing boundaries. While Silver-Müller boundary conditions can be applied as described above, they are only of first order and insufficient for the accurate modeling of open systems. Thus, they need to be complemented by Perfectly Matched Layers (PMLs, see e.g. Refs. [4,16]). In Ref. [16], Lu et al. demonstate how to properly implement uniaxial PMLs in two dimensions within a DG framework. To extend their work to fully three-dimensional systems, we start from the general uniaxial formulation [4,17], where one describes a PML region as a dispersive, anisotropic material with susceptibility tensor $\underline{\underline{\epsilon}} = \epsilon\underline{\underline{\Lambda}}$ and permeability tensor $\underline{\underline{\mu}} = \mu\underline{\underline{\Lambda}}$. Here, the diagonal

tensor $\underline{\underline{\Lambda}}$ is explicitly given by

$$\underline{\underline{\Lambda}} = \begin{pmatrix} \frac{s_y s_z}{s_x} & 0 & 0 \\ 0 & \frac{s_x s_z}{s_y} & 0 \\ 0 & 0 & \frac{s_x s_y}{s_z} \end{pmatrix} \quad \text{with} \tag{8}$$

$$s_m = 1 + \frac{\sigma_m}{i\omega}, \quad m \in \{x, y, z\}.$$

Upon transforming Maxwell's equations to the frequency domain and inserting the anisotropic material parameters we obtain

$$i\omega\epsilon\underline{\underline{\Lambda}}\breve{\vec{E}} = \nabla \times \breve{\vec{H}}, \tag{9}$$

$$-i\omega\mu\underline{\underline{\Lambda}}\breve{\vec{H}} = \nabla \times \breve{\vec{E}}, \tag{10}$$

where '$\breve{}$' denotes the variables in frequency domain. For brevity, we limit the discussion to the first component of $\vec{E}$, which reads

$$i\omega\epsilon\breve{E}_x = -\frac{\partial}{\partial y}\breve{H}_z + \frac{\partial}{\partial z}\breve{H}_y - \underbrace{i\omega\epsilon\left(\frac{s_y s_z}{s_x} - 1\right)\breve{E}_x}_{=:\breve{J}_x}. \tag{11}$$

The newly introduced polarization current $\breve{J}_x$ can be further simplified to

$$\breve{J}_x = \frac{i\omega\epsilon}{i\omega + \sigma_x}\left(\sigma_y + \sigma_z - \sigma_x + \frac{\sigma_y\sigma_z}{i\omega}\right)\breve{E}_x. \tag{12}$$

By introducing the new variable $\breve{P}_x = \breve{J}_x - \epsilon(\sigma_y + \sigma_z - \sigma_x)\breve{E}_x$, we obtain the expression

$$i\omega\breve{P}_x = -\sigma_x\breve{P}_x + \epsilon(\sigma_x^2 + \sigma_y\sigma_z - \sigma_y\sigma_x - \sigma_z\sigma_x)\breve{E}_x, \tag{13}$$

which can now be transformed back to the time-domain. The resulting coupled equations then take on the form

$$\frac{\partial}{\partial t}E_x = -\frac{\partial}{\partial y}H_z + \frac{\partial}{\partial z}H_y - \epsilon(\sigma_y + \sigma_z - \sigma_x)E_x - P_x, \tag{14}$$

$$\frac{\partial}{\partial t}P_x = -\sigma_x P_x + \epsilon(\sigma_x^2 + \sigma_y\sigma_z - \sigma_y\sigma_x - \sigma_z\sigma_x)E_x. \tag{15}$$

The derivation of corresponding auxiliary differential equations (ADEs) for the other field components is completely analogous. At this point, we would like to note that the widths of the layers and their strengths σ_m are free parameters that have to be optimized for best performance.

A second important point is the excitation of the system through sources. Besides via initial conditions, there are two conceptually different ways to inject radiation into the system. The more obvious path is to add current density terms to Eqs. (5) and (6). An alternative is given by the so-called Total-Field/Scattered-Field approach (TF/SF, see e.g. Ref. [4] for a detailed discussion). Typically, the current density is more suitable to introduce localized sources while the TF/SF method can be employed to inject plane waves. Within the DG framework, one can easily implement the TF/SF approach by modifying the field differences in the numerical fluxes. The addition of current terms also presents no fundamental problem, but the spatial profile is obviously expanded into Lagrange polynomials. For the very important case of a delta-like point source, this expansion becomes rather intricate and a highly refined mesh around the source is required to model it accurately. In turn, this dramatically reduces the computational performance due to the stability criterion (7). Therefore, we propose to implement point sources by exploiting the TF/SF method. For the injection, a small contour around the desired source location is embedded into the mesh and the outer area is defined as the TF region. The required fields on the contour can be obtained by means of Green's functions similar to the discussion in Ref. [18]. For the two-dimensional case in TM-polarization and using polar coordinates, the fields generated by a point source at the origin can be expressed as

$$E_z(\rho, \varphi, t) = \frac{1}{2\pi}\int_\rho^t \mathrm{d}\tau \frac{j'(t-\tau)}{\sqrt{\tau^2 - \rho^2}}, \tag{16}$$

$$H_x(\rho, \varphi, t) = \frac{\cos(\varphi)}{2\pi\eta\rho}\int_\rho^t \mathrm{d}\tau \frac{\tau j'(t-\tau)}{\sqrt{\tau^2 - \rho^2}}, \tag{17}$$

$$H_y(\rho, \varphi, t) = -\frac{\sin(\varphi)}{2\pi\eta\rho}\int_\rho^t \mathrm{d}\tau \frac{\tau j'(t-\tau)}{\sqrt{\tau^2 - \rho^2}}, \tag{18}$$

were $j(t)$ is the time-dependence of the source and $j'(t)$ denotes its derivative with respect to the argument. The above integrals exhibit a singularity at the left limit $\tau = \rho$. However, when employing an appropriate quadrature rule [19], it becomes possible to numerically obtain values at arbitrary locations with sufficiently high accuracy.

A third extension is the implementation of dispersive materials. For the DG method, an auxiliary differential equations (ADEs) formulation [4] appears to be the most natural choice. Here, we will focus on the modeling of silver, which in the visible frequency range is well described by a Drude model [20]. The

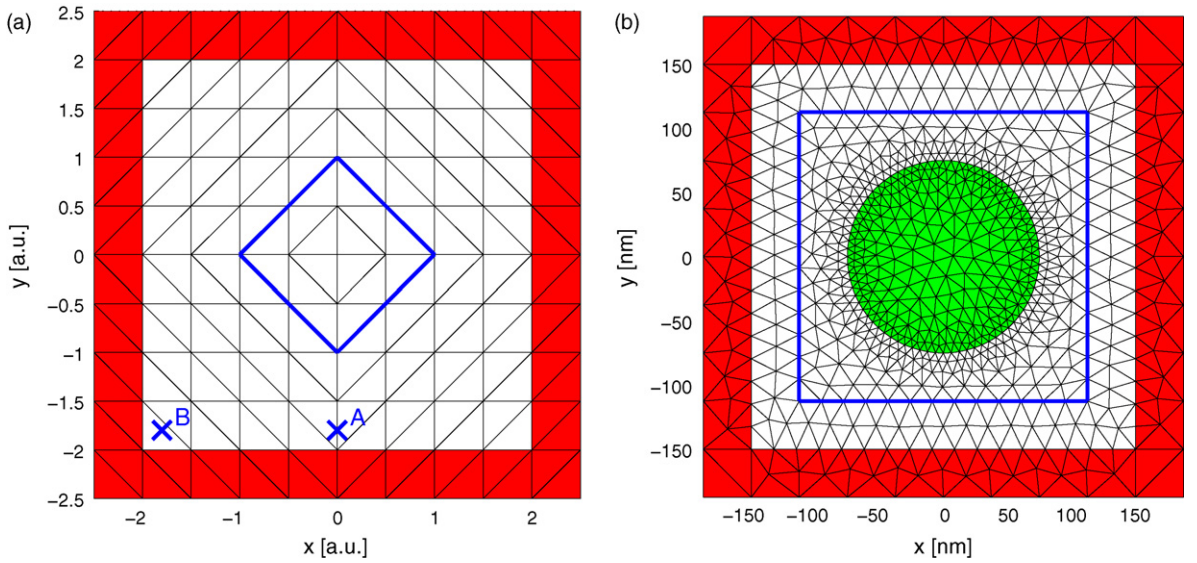

Fig. 1. Meshes used for the validation of PMLs. In both cases, the red shaded areas are the PML regions and the blue lines indicate TF/SF contours. In panel (a), the mesh used for exploring the influence of the absorption grading on the PMLs is shown. The two crosses denote points $A(0,-1.8)$ and $B(-1.8,-1.8)$ where the fields are recorded for comparison. The panel (b) depicts the mesh used for the calculation of scattering cross sections. Here, the TF/SF contour also serves for the flux integration. In total, this mesh consists of 1506 triangles. (For interpretation of the references to color in this figure legend, the reader is referred to the web version of the article.)

corresponding frequency-dependent permittivity is given by

$$\epsilon(\omega) = 1 - \frac{\omega_{\mathrm{pl}}}{\omega(\omega + i\omega_{\mathrm{col}})}, \tag{19}$$

where ω_{pl} and ω_{col} denote, respectively, the plasma and collision frequency. The derivation of the ADEs for the Drude model is well documented [4,15,21] and leads to additional equations, one per spatial dimension, that complement Maxwell's equations

$$\frac{\partial}{\partial t}\vec{j}_{\mathrm{Drude}} = \omega_{\mathrm{pl}}^2 \vec{E} - \omega_{\mathrm{col}}\vec{j}_{\mathrm{Drude}}. \tag{20}$$

As long as the material parameters are constant for each element Ω^k, the inclusion of the corresponding auxiliary equations is straightforward.

4. Optimization of PML parameters and comparison with FDTD

As alluded to above, the PMLs contain a free parameter σ which needs to be determined numerically for best performance. In the case of FDTD, extensive numerical studies [4] have shown that optimal performance is obtained when making σ position dependent. A typical choice is the polynomial grading

$$\sigma(x) = (x/d)^m \sigma_{\max},$$

where d is the thickness of the PML-layer while m and $\sigma_{\max}$ are free parameters. Best results are obtained for values of $m \approx 3-4$ and $\sigma_{\max} \approx ((m+1)/2d)R$, where R is a number of the order 10. To facilitate a comparison of our PMLs in the DG method with those of FDTD, we adopt the same polynomial grading with free parameters m and R. In order to scan the entire parameter space, we use a small two-dimensional test system in TM-polarization as sketched in Fig. 1(a). A point-source is placed in the center of the system and is injected via a TF/SF contour as discussed in the previous section. The temporal shape of the source is chosen to be a differentiated Gaussian pulse $j(t) = -(t-t_0)/t_{\mathrm{w}}^2 \exp\left(-(t-t_0)^2/(2t_{\mathrm{w}}^2)\right)$ with parameters $t_{\mathrm{w}} = 0.5$ and $t_0 = 5$. At this point, we would like to note that we are using dimensionless units and all simulations have been run for a total simulation time of $T = 30$. During the calculation, the field values E_z are recorded for two distinct points, A and B (marked as crosses in Fig. 1(a)). Afterwards this data is compared to the semi-analytic solution E_z^{ref} obtained from numerical integration of Eq. (16). As a measure for the relative error we use

$$\mathcal{E}_{\mathrm{rel}} = \frac{\max_t(|E_z^{\mathrm{ref}} - E_z|)}{\max_t(E_z^{\mathrm{ref}})}. \tag{21}$$

In Fig. 2, we display the results of our parameter studies for the system sketched in Fig. 1(a) as well as for a setup

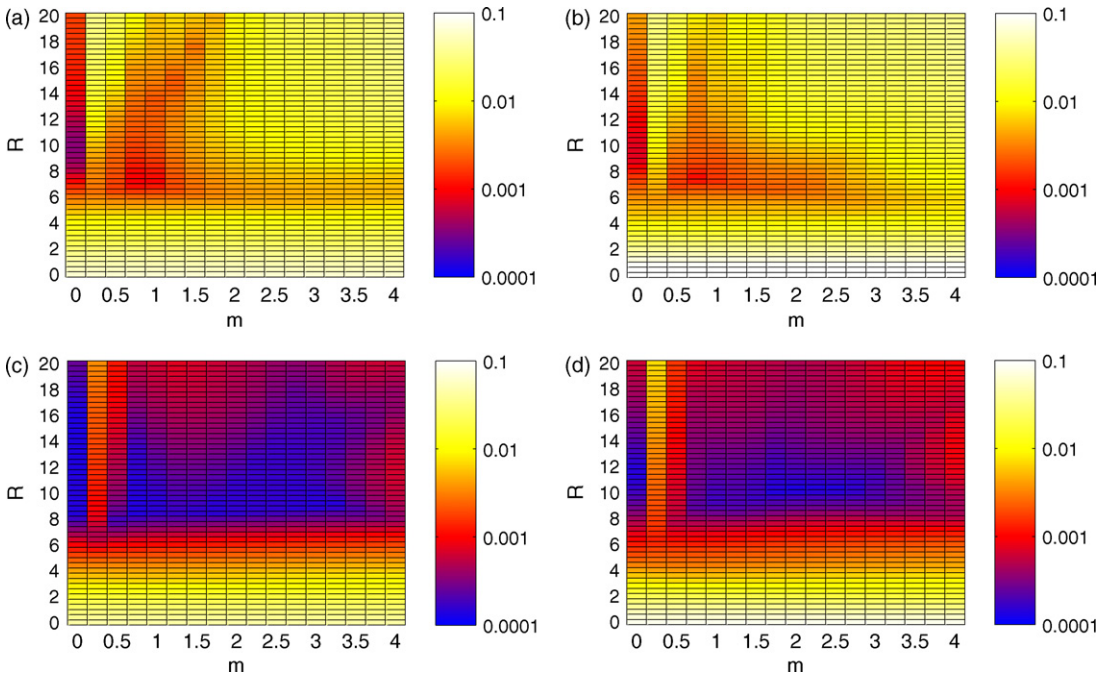

Fig. 2. Dependence of the relative error at points A and B on the parameters m and R for two different systems of PMLs. Panels (a) and (b) depict the error for a single layer of PMLs as displayed in Fig. 1. In panels (c) and (d), a second layer of PMLs is added around the system. Panels (a) and (c) show the error at point A, while panels (b) and (d) corresponds to data recorded at point B.

with two layers of PMLs around it. In both cases, we used a 4th-order discretization. Most importantly, we note that for our system with only one layer of PMLs, we already achieve a relative error below 10^{-3}. Further, this minimum does not coincide with the one expected from FDTD. Instead, the best performance can be observed for $m = 0$ which renders the grading obsolete. Adding a second layer improves the performance by roughly one order of magnitude and makes the system less sensitive to the parameters m and R. While we still observe the best performance for $m = 0$, the range of m between 1 and 3 now yields similar results. From studying a multitude of different systems using different numbers of elements as well as different polynomial orders (not shown here), we conclude that a minimum at $m = 0$ is a rather universal feature.

A more detailed look at the performance for $m = 0$ is presented in Fig. 3, where the maximal error is plotted

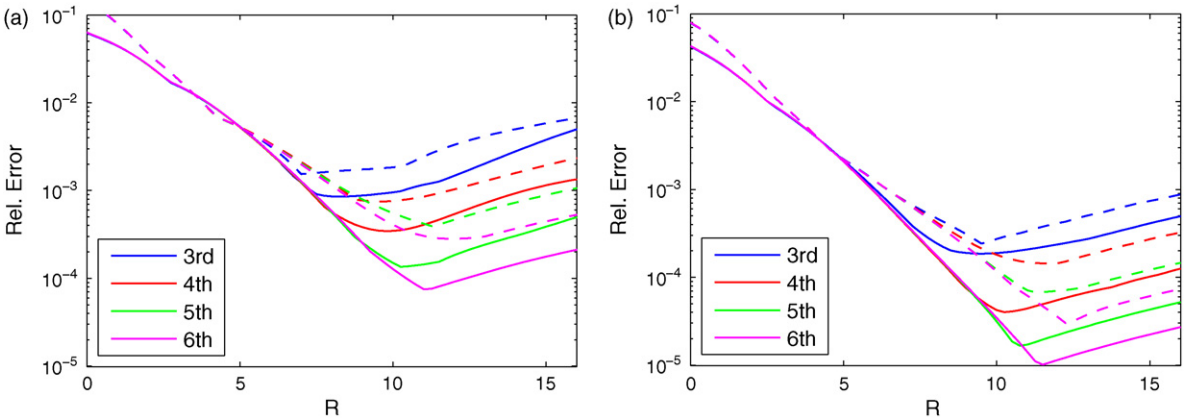

Fig. 3. Performance of the PMLs for $m = 0$ as a function of the parameter R. The colors denote different expansion orders, while the linestyles correspond to points A (solid) and B (dashed). In panel (a) the data for the system with a single layer of PMLs around is shown, while panel (b) contains the results for a system with two layers. (For interpretation of the references to color in this figure legend, the reader is referred to the web version of the article.)

as a function of R. In contrast to the previous results, we now compare the recorded fields against those obtained numerically in a much larger system. This allows us to focus on the errors caused by spurious reflection at the PMLs. From these extensive numerical studies we conclude that a flat absorption profile yields similar or better results than the polynomial grading usually employed in FDTD. Further, for most applications it is sufficient to only use a single cell of PMLs around the system and for optimal performance one should choose $R \approx 10$. Preliminary studies indicate that most of these conclusions also hold for three-dimensional systems.

To further validate our implementation of the DG technique and to compare it to the FDTD method, we study the cross section of an infinitely extended metallic cylinder for the case of TE-polarization, where analytic solutions are available via Mie theory [22]. The schematic setup is shown in Fig. 1(b), where a plane-wave impinges onto a metallic cylinder with radius $r = 75$ nm. The metal is incorporated via a Drude model with parameters $\omega_{\mathrm{pl}} = 1.39 \times 10^{16}\ \mathrm{s}^{-1}$and $\omega_{\mathrm{col}} = 3.23 \times 10^{13}\ \mathrm{s}^{-1}$[20]. The scattering cross sections are then obtained by integrating the Poynting vector along a closed contour around the cylinder. From the data in Fig. 4, one can clearly see that the FDTD method yields spurious oscillations, while the DG results are in perfect agreement with the analytical results. The poor performance of the FDTD method in this case is a direct consequence of the stair-casing approximation, which supports unphysical surface modes [23]. Due to the unstructured mesh used in the DG case, one can locally refine the discretization at the surface and, therefore, obtain highly accurate results with only few triangles. In the present case, we use a mesh with 1506 triangles which has been generated using NETGEN [24]. Employing a 5th order polynomial expansion amounts to a total of 31626 grid points. These are more than two orders of magnitude fewer points than what is required for a similarly converged FDTD calculation. Hence, despite the increased computational effort per grid point, the DG method can outperform the FDTD scheme, both in CPU-time and memory consumption, when an accurate modeling of geometrical features is mandated.

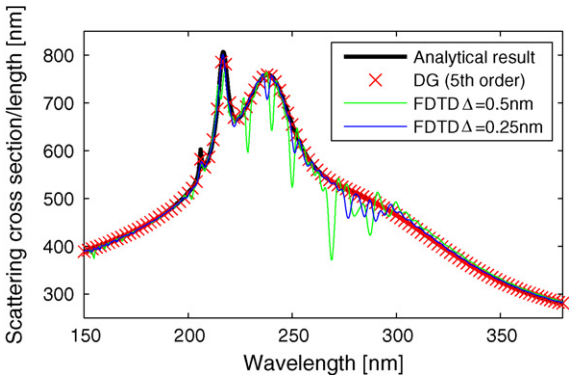

Fig. 4. Scattering cross section of a silver cylinder with radius $r = 75$ nm. The analytic reference solution (black line) has been obtained via Mie theory.

5. Transmission through subwavelength apertures

While extraordinary transmission through individual subwavelength apertures has attracted a lot of attention in the past years, most theoretical work is still based on approximations that describe the metal as a perfect electric conductor (PEC) [25,26]. Although this simplifies the calculations and may provide a qualitative picture of the physical processes, it is not suitable for designing and optimizing experiments. As an application of the DGTD approach we will, in the following, study the influence of a more accurate description of the material on the transmittance properties of such apertures. A typical structure is sketched in Fig. 5 and consists of an infinite metallic screen of thickness w with a nano-structured surface. We assume a slit of width a going through the metal and next to it N grooves of width a and depth h that are spaced a distance d apart from each other. The many parameters make it obvious, that a fast and reliable numerical method is required to thoroughly study the properties of such systems. Although these structures can be grid-aligned and, thus be treated with FDTD, the DG method still exhibits a distinct advantage: The unstructured meshes allow an accurate resolution of the small nano-structures without wasting grid points in the bulk regions. Specifically, we employ a 4th-order discretization in all forthcoming calculations.

Before getting to the full structure we first analyze the simple slit aperture without grooves so as to obtain a reference. We assume a metallic film of thickness

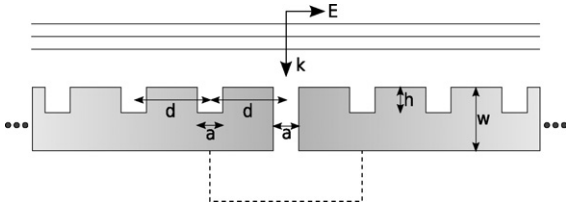

Fig. 5. Schematic setup of a slit aperture in a metallic film. The aperture is flanked by a finite number of grooves and the dashed line indicates a contour used to calculate the transmittance.

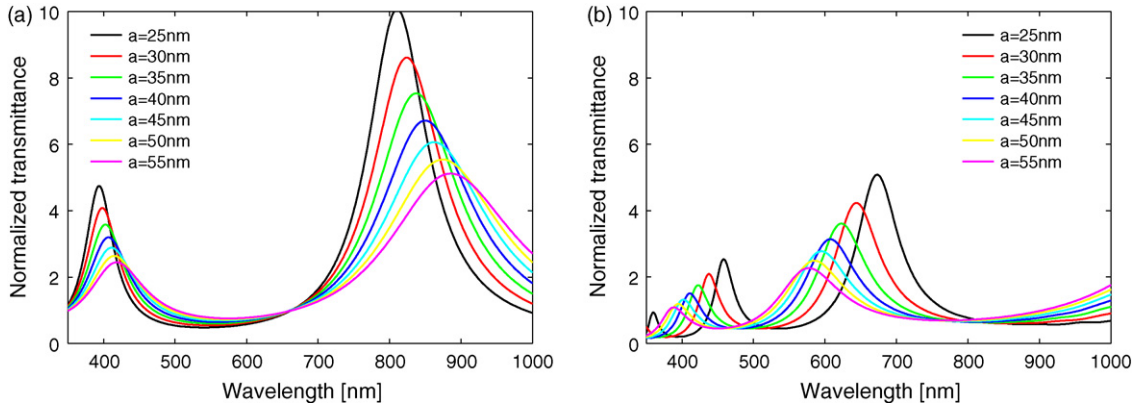

Fig. 6. Normalized transmittance spectra for simple apertures with different slit widths a. In panel (a) the spectra for systems with perfectly conducting metal are shown, while panel (b) contains the results for metallic systems that are described by a Drude model (see text for details).

$w = 350$ nm with a single slit of width a and irradiate it with a plane wave, where the magnetic field is parallel to the slit. The pulse shape is taken to be a broadband Gaussian with a carrier wavelength of $\lambda_0 = 500$ nm that covers the relevant spectrum from 350 nm to 1000 nm. Behind the aperture, we integrate the flux over the entire half-space and normalize it to the width of the aperture. First, we conduct a series of calculations with different slit width a for both, a PEC structure as well as for a more realistic Drude model with silver parameters $\omega_{\mathrm{pl}} = 1.37 \times 10^{16}\ \mathrm{s}^{-1}$ and $\omega_{\mathrm{col}} = 8.5 \times 10^{13}\ \mathrm{s}^{-1}$[27]. We display the results in Fig. 6. Already for the simple slit aperture, the differences between PEC and a Drude metal are quite significant. For the realistic metal, the transmission is reduced, which is consistent with the fact that the silver exhibits absorption through an imaginary part in the dielectric function. Further, the position of the resonance at higher wavelength is strongly blue-shifted for the Drude case. Finally, for both material models the resonances shift with varying slit width a, but they move in opposite directions. For the PEC structure, the resonances shifts to longer wavelengths as a increases, while they move towards shorter wavelengths when the Drude model is used to describe the metal.

We now proceed to the full structures with added grooves, and again start the analysis by comparing the PEC and the Drude model. The geometrical parameters are fixed to $d = 500$ nm, $h = 100$ nm, $w = 350$ nm, and $a = 40$ nm, identical to those reported in Ref. [26]. As discussed above, a simple slit shows two pronounced resonances, while adding the corrugation gives rise to a third peak with significantly increased transmittance. Our data for the PEC structure is in perfect agreement with results obtained via the modal expansion technique (c.f. Fig. 2(a) in Ref. [26]). By comparing the data in Fig. 7(a) and (b), we again observe the strong influence of the material model on the spectra. In addition to the resonance shifts observed before, for the PEC case, the

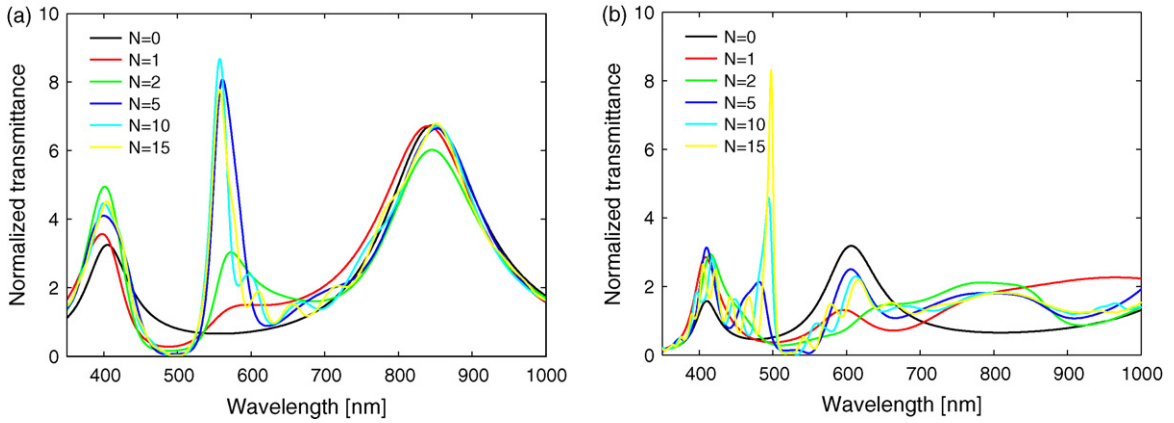

Fig. 7. Normalized transmittance spectra for slit apertures with added grooves for different numbers of grooves. The geometrical parameters are $d = 500$ nm, $h = 100$ nm, $w = 350$ nm, and $a = 40$ nm. Panel (a) depicts the spectra for systems with perfectly conducting metal, while in panel (b) the metal is described by a more realistic Drude model.

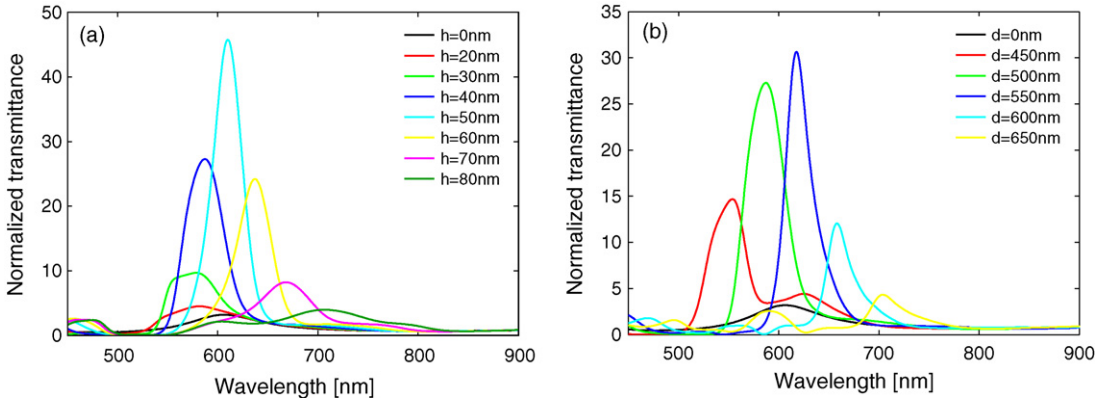

Fig. 8. Normalized transmittance spectra for different parameters of the corrugations. In (a) the variation with the groove depth h is shown, while in (b) the results of changing the distance d between the grooves are displayed.

central resonance quickly saturates for $N \approx 5$ grooves. When using the Drude model, around $N = 15$ grooves are required to observe a similar enhancement.

In a next step, we want to study the influence of the groove depth h and the spacing d between the grooves on the systems' transmittance properties. In accordance with the experimental setup in Ref. [26], we fix the number of grooves to $N = 5$ and keep all other parameters identical to those of the previous calculations expect for the height h, which is now scanned from $h = 20$ nm to $h = 80$ nm. All calculations are carried out with the more realistic Drude model. From the results depicted in Fig. 8(a), we deduce that changing the height results in a shift of the central resonance. The highest transmittance is observed, when this central resonance coincides with a peak of the simple aperture at 610 nm (see Fig. 6(b)). The results for scanning the distance d between the grooves display a similar behavior as shown in Fig. 8(b). Here, we have fixed the depth to $h = 40$ nm and changing d again leads to shifts of the central resonance frequency. As before, one observes that the maximum transmittance is reached when the resonance coincides with the resonance of the simple aperture.

6. Conclusion

In conclusion, we have demonstrated how the discontinuous Galerkin method can be employed to study the optical response of metallic nano-structures. Through the development of important add-ons such as optimized PMLs and point sources, the DG method acquires the same versatility as standard methods such as FDTD. Most importantly, through its ability to work on conforming meshes and the higher-order spatial accuracy, the DG method exhibits distinct advantages over FDTD. We have exploited those features to study certain aspects of the phenomenon of extraordinary transmission through nano-structured metallic films. In particular, we have demonstrated the importance of modeling the metal as a dispersive material and we have studied the sensitivity to the system's geometrical parameters. In order to further enhance the performance of the DG method, great potential lies in the time integration scheme. So far, we have employed a simple and efficient low-storage Runge–Kutta technique. However, unconditionally stable methods such as those presented in Refs. [4,14,15] should allow larger time steps and should lead to significantly faster calculations.

Acknowledgements

We acknowledge financial support by the Center for Functional Nanostructures (CFN) of the Deutsche Forschungsgemeinschaft (DFG) within subproject A1.2. The research of JN and MK is further supported through the Karlsruhe School of Optics & Photonics (KSOP) at the Universität Karlsruhe. MK also acknowledges financial support for his stay abroad by the Karlsruhe House of Young Scientists.

References

[1] E. Ozbay, Plasmonics: merging photonics and electronics at nanoscale dimensions, Science 311 (2006) 189–193.
[2] K. Busch, G. von Freymann, S. Linden, S.F. Mingaleev, L. Tkeshelashvili, M. Wegener, Periodic nanostructures for photonics, Phys. Rep. 444 (2007) 101–202.
[3] F.J. García de Abajo, Light scattering by particle and hole arrays, Rev. Modern Phys. 79 (2007) 1267–1290.
[4] A. Taflove, S.C. Hagness, Computational Electrodynamics: The Finite-Difference Time-Domain Method, Third Edition, Artech House Publishers, 2005.
[5] A. Farjadpour, D. Roundy, A. Rodriguez, M. Ibanescu, P. Bermel, J.D. Joannopoulos, S.G. Johnson, Improving accuracy

by subpixel smoothing in the finite-difference time domain, Opt. Lett. 31 (2006) 2972–2974.
[6] A. Deinega, I. Valuev, Subpixel smoothing for conductive and dispersive media in the finite-difference time-domain method, Opt. Lett. 32 (2007) 3429–3431.
[7] A. Mohammadi, T. Jalali, M. Agio, Dispersive contour-path algorithm for the two-dimensional finite-difference time-domain method, Opt. Express 16 (2008) 7397–7406.
[8] A.-K. Tornberg, B. Engquist, Consistent boundary conditions for the Yee scheme, Journal of Computational Physics 227 (2008) 6922–6943.
[9] J. Jin, Computational Electrodynamics: The Finite Element Method in Electromagnetics, Second Edition, John Wiley & Sons, 2002.
[10] J. Hesthaven, T. Warburton, Nodal high-order methods on unstructured grids—I. Time-domain solution of Maxwell's equations, J. Comput. Phys. 181 (1) (2002) 186–221.
[11] T. Warburton, An explicit construction of interpolation nodes on the simplex, J. Eng. Math. 56 (3) (2006) 247–262.
[12] M.H. Carpenter, C.A. Kennedy, Fourth-Order 2N-Storage Runge–Kutta Schemes, Tech. Re NASA-TM-109112, NASA Langley Research Center, VA, June 1994.
[13] A. Kanevsky, M.H. Carpenter, D. Gottlieb, J.S. Hesthaven, Application of implicit–explicit high order Runge–Kutta methods to discontinuous-Galerkin schemes, J. Comput. Phys. 225 (2) (2007) 1753–1781.
[14] J. Niegemann, L. Tkeshelashvii, K. Busch, Higher-order time-domain simulations of Maxwell's equations using Krylov-subspace methods, J. Comput. Theor. Nanos. 4 (3) (2007) 627–634.
[15] K. Busch, J. Niegemann, M. Pototschnig, L. Tkeshelashvili, A Krylov-subspace based solver for the linear and nonlinear Maxwell equations, Phys. Status Solidi B 244 (10) (2007) 3479–3496.
[16] T. Lu, P. Zhang, W. Cai, Discontinuous Galerkin methods for dispersive and lossy Maxwell's equations and PML boundary conditions, J. Comput. Phys. 200 (2) (2004) 549–580.
[17] Z. Sacks, D. Kingsland, R. Lee, J. Lee, A perfectly matched anisotropic absorber for use as an absorbing boundary condition, IEEE Trans. Antennas Propagat. 43 (12) (1995) 1460–1463.
[18] R. Nevels, J. Jeong, The time domain Green's function and propagator for Maxwell's equations, IEEE T. Antenn. Propag. 52 (11) (2004) 3012–3018.
[19] W. Press, S. Teukolsky, W. Vetterling, B. Flannery, Numerical Recipes in C, 2nd Edition, Cambridge University Press, Cambridge, UK, 1992.
[20] P.B. Johnson, R.W. Christy, Optical constants of the noble metals, Phys. Rev. B 6 (12) (1972) 4370–4379.
[21] X. Ji, W. Cai, P. Zhang, High-order DGTD methods for dispersive Maxwell's equations and modelling of silver nanowire coupling, Int. J. Numer. Methods Eng. 69 (2) (2007) 308–325.
[22] C.F. Bohren, D.R. Huffman, Absorption and Scattering of Light by Small Particles, 2nd Edition, John Wiley & Sons, New York, USA, 1983.
[23] A.C. Cangellaris, D.B. Wright, Analysis of the numerical error caused by stair-stepped approximation of a conducting boundary in FDTD Simulations of Electromagnetic Phenomena, IEEE Trans. Antennas Propagat. 39 (10) (1991) 1518–1525.
[24] J. Schöberl, Netgen an advancing front 2d/3d-mesh generator based on abstract rules, Comput. Visual Sci. 1 (1) (1997) 41–52.
[25] Y. Takakura, Optical resonance in a narrow slit in a thick metallic screen, Phys. Rev. Lett. 86 (24) (2001) 5601–5603.
[26] F.J. García-Vidal, H.J. Lezec, T.W. Ebbesen, L. Martín-Moreno, Multiple paths to enhance optical transmission through a single subwavelength slit, Phys. Rev. Lett. 90 (21) (2003) 213901.
[27] G. Dolling, C. Enkrich, M. Wegener, C.M. Soukoulis, S. Linden, Low-loss negative-index metamaterial at telecommunication wavelengths, Opt. Lett. 31 (12) (2006) 1800–1802.